Energy Harvesting Long-Range Marine Communication

Ali Hosseini-Fahraji, Pedram Loghmannia, Kexiong Zeng, Xiaofan Li, Sihan Yu, Sihao Sun, Dong Wang, Yaling Yang, Majid Manteghi, and Lei Zuo
Bradley Department of Electrical and Computer Engineering, Virginia Tech, Blacksburg, VA, USA
{alih91, pedraml, kexiong6, lixf, shy, sihaosun, dong0125, yyang8, manteghi, leizuo}@vt.edu

***Abstract*—This paper proposes a self-sustaining broadband long-range maritime communication as an alternative to the expensive and slow satellite communications in offshore areas. The proposed system, named Marinet, consists of many buoys. Each of the buoys has two units: an energy harvesting unit and a wireless communication unit. The energy harvesting unit generates electrical energy from ocean waves to support the operation of the wireless communication unit. The wireless communication unit on each buoy operates in a TV white space frequency band and connects to each other and wired high-speed gateways on land or islands to form a mesh network. The resulting mesh network provides wireless access services to marine users in their range. A prototype of the energy harvesting unit and the wireless communication unit are built and tested in the field. In addition, to ensure Marinet will maintain stable communications in rough sea states, an ocean-link-state prediction algorithm is designed. The algorithm predicts ocean link-states based on ocean wave movements. A realistic ocean simulator is designed and used to evaluate how such a link-state prediction algorithm can improve routing algorithm performance.**

***Index Terms*—Marinet, white space, energy harvesting, maritime communication, ocean-link-state prediction algorithm**

I. Introduction

Thanks to the extensive land-based cellular and Wi-Fi wireless network coverages, mobile broadband connectivity from tens to hundreds of Mbps has been taken for granted in many aspects of our daily lives and industrial operations. However, there are no high-speed connections for people and industries in the ocean. When one moves several miles away from the coast into the sea, cellular coverage starts to fade away, and Wi-Fi signals are non-existence. Yet, the existing choices of mobile marine communication technologies are severely lagging behind their land counterparts. The existing maritime communication services used in the ocean can be divided into three kinds. The first type is satellite communications, which are available almost everywhere in the world, and can provide wireless services to both static and mobile vessels. However, satellite services are expensive, with limited bandwidth and extremely long delays [1], [2]. For instance, a typical portable satellite service has an up-front hardware cost of $2000–$60,000 and a monthly charge of $50–$100 for an average link speed of 100 kbps and a few MB of monthly data communication quota. As a result, the services it provides are limited to "text email, downloading weather GRIB files (usually <15K bit), and emergency web-browsing on very small web pages" [3]. Given the fact that the current average size of a webpage is more than 2 MB [4] and is still growing, even common web-browsing is painfully slow through this technology. The second option is MF, HF, or VHF ship-to-shore radios, which only support voice communications because of their limited bandwidth (<38.4 kbps typically [5]). The third kind is undersea fiber. Although this technology provides a high-speed connection to fixed marine sites, the deployment cost is extremely high (roughly $100k/km [6]).

As maritime communications are severely lagging behind their land counterparts, many network applications that are commonly seen on the land are not possible in the ocean. For example, marine workers are not able to read online manuals with lots of pictures, watch short online tutorial videos, or engage in web teleconferencing with their colleagues when they run into technical issues at sea. Control centers on land are unable to monitor marine surveillance video or stream sensing data in real-time. Cruise passengers can not browse most websites, watch online movies or TV, and have a video chat. Essentially, ships, oil-rigs, ocean sensors, autonomous underwater vehicles, and all the industry and people working around them are in critical need of a new marine communication infrastructure to provide them with mobile broadband connectivity to the rest of the world. Such an infrastructure can significantly improve the safety, flexibility, manageability, and efficiency of these ocean entities and the quality of life of marine workers and tourists.

In order to provide low-cost, low-maintenance, and high-speed connectivity on the ocean, we face three unique challenges. First, communication base-stations on land are usually mounted on high-altitude sites such as mountains, tall buildings, and specialized communication towers. However, such places are usually not available on the ocean. Second, while the power supply for communication infrastructures on land can be transmitted directly through power lines, such standard power supply does not exist on the ocean. Finally, on land, communication infrastructures are connected directly to the Internet via cables, but such cable connections are not available on the ocean.

To address the above challenges, in this paper, we explore the idea of *Marinet*, an energy harvesting maritime mesh network. As shown in Fig. 1, a Marinet node consists of two units, which are an energy harvesting buoy and a wireless base-station mounted on the buoy. The 0.7-meter-diameter energy harvesting buoy is compact, low-cost, and

low-maintenance, which can be mass-produced and dropped into water with low deployment cost. The buoy can harvest energy from the ocean wave by taking advantage of the relative motion between the floating buoy and the submerged body, which provides the energy source to support the wireless communication services of the base-station. The base-station on a buoy maintains high-speed wireless connections with neighboring buoys, which form a self-organized mesh network. The mesh network is connected to gateways, which have high-speed fiber connections to the Internet and can either be mounted on the shore or any fixed infrastructures in the ocean. The buoys are anchored to the seafloor to ensure the stability of the mesh network. In this way, we can solve the challenges of base-station placement and power supply by using floating base-stations and energy harvested from the ocean. Meanwhile, by leveraging multi-hop wireless links, the lack of cable connection is resolved. Therefore, combining the floating base-stations, sustainable power harvested from the ocean, and multi-hop wireless links, Marinet can provide low-cost, high-speed connectivity to various maritime applications. Such a wireless mesh network covering offshore areas will satisfy the vast majority of the communication needs for ships and oil platforms in the ocean.

The purpose of this paper is to provide a proof of concept for such a Marinet system by developing and evaluating the key units of such a system. Specifically, a brief description of the energy harvesting buoy and its expected power generation is presented in Section III. Section IV is dedicated to the design of wireless radios for marine communications. Then, the challenges and their feasible solutions in the mesh network design are considered in Section V. The evaluation of the system based on field measurement data and simulation is discussed in Section VI. This paper is concluded in Section VII.

II. Related Work

Some of the recent efforts to address marine communication problems include the Google Loon project and the Facebook Aquila project. The Loon project attempts to provide internet connectivity through mesh networks formed by balloons. Yet, it faces severe safety and reliability issues. The balloons have a short life span of 100 days and move by wind currents. Failure in balloon control causes mid-air collision with other aircraft, unwanted balloon landings affecting human life, and unpredictable landing places for future maintenance. In addition, predicting balloon routes and monitoring balloons in real-time motion require a huge database and complex programming to generate mesh networking and provide reliable communication. The Aquila project intends to use solar-powered drones as relay stations. However, it was halted after 4 years in June 2018 because landing the super-sized Aquila drones turned out to be a huge challenge.

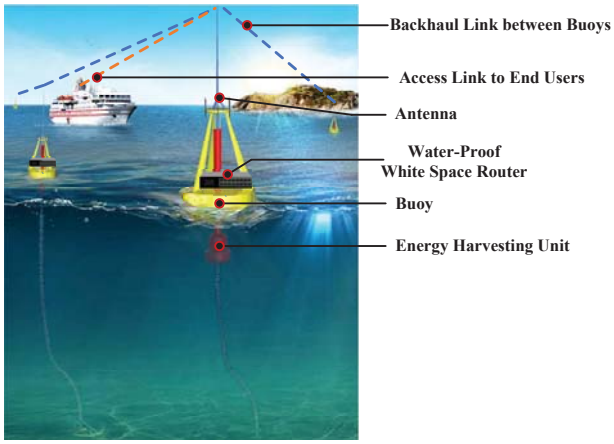

Fig. 1. Illustration of Marinet.

III. Energy Harvesting Buoy

The energy harvesting buoy is the cornerstone of the entire system, since using long cables to access land power is extremely costly. Although solar power is easy to harvest, it is not stable due to night time, weather, and seasonal factors. In addition, when operating in the ocean, solar panels require regular cleaning due to the growth of marine organisms (*e.g.*, barnacles, algae, etc.) on them. Thus, in our work, we designed ocean-wave energy harvesting units for the buoys so that our buoys can consistently harvest large enough amounts of power to support communication services. By measurements taken in both the ocean and wave tank, the buoy is predicted to continuously generate electrical power in tens or hundreds of watts from ocean waves (*e.g.*, 76–306 W for 0.5–1 m wave height that falls into sea state 2–3). Moreover, wave energy is very stable compared to solar panels and less affected by light/weather conditions. With such a high and stable energy supply, energy harvesting buoys can provide sustainable power to networking devices. Also, since the energy harvesting unit is enclosed in a water-tight case, it will not suffer from the growth of marine organisms and hence is low-maintenance.

A. Design and Testing of the Two-Body Self-React Ocean Wave Energy Converter

As shown in Fig. 1, the energy harvesting unit known as wave energy converter (WEC) contains two bodies: a floating buoy moving up and down with ocean waves, and a submerged body in a certain ocean depth. The bi-directional up and down motions of the floating buoy converts into uni-directional motions to drive the generator to produce electricity. Fig. 2 illustrates the design of the WEC, which is designed to achieve the self-react effect and catch up with the low excitation frequency of the ocean wave. The theoretical analysis and detailed description of the two-body design can be found in [7], [8]. This two-body system has a relative heave motion under wave excitation, which is directly transferred through a set of the ball screw and ball nut into the power take-off (PTO). Based on a mechanical motion rectifier (MMR) mechanism, the power take-off can rectify the reciprocating rotation of the ball screw into a single directional rotation, then drive a permanent-magnetic generator to provide the electricity that power other devices [9]. Through dry laboratory tests, as shown in Fig. 3, we identified and characterized the overall WEC with the MMR PTO, where an accurate model between the harvested energy and the water surface displacement is

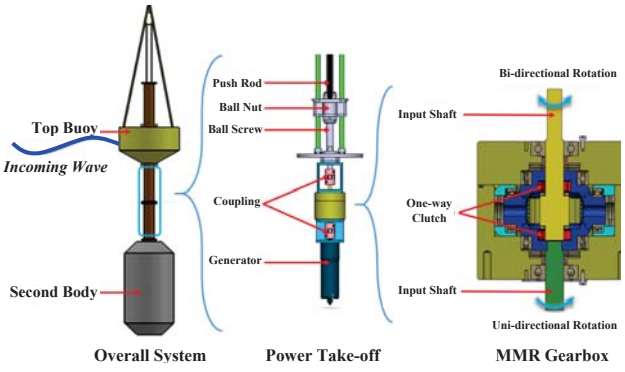

Fig. 2. Design details of the WEC and PTO.

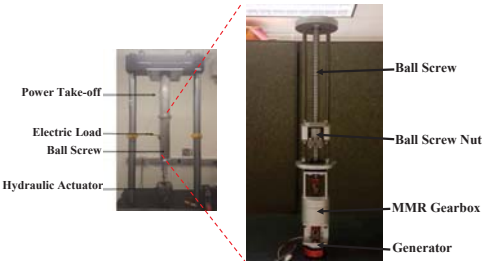

Fig. 3. Dry lab testing of the PTO prototype.

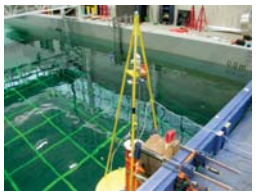

Fig. 4. Water tank test.

established. We then compare the model with real test results in a water tank, as illustrated in Fig. 4, where a series of waves with specified wave parameters are generated. Fig. 5 compares the water tank test results with simulations that are based on the characterization model. Our model matches well with real test results, indicating that through reasonable system identification and characterization, the performance of the proposed WEC can be well predicted. Since wave power is proportional to the wave height square and wave period, with sufficient knowledge of the wave coming to the WEC, the total energy to be generated can be forecast, and pre-planning for the power usage is applicable [10].

B. Average Power Generation Analysis

Given the model of our WEC mentioned in Subsection III-A, based on the profile of real ocean waves, we can estimate the maximum, average, and minimum energy that can be generated for a given time period in the ocean. Specifically, the wave profile shown in Fig. 6 is acquired from the NOAA buoy center [11], which shows the significant wave heights over a year. Here, significant wave height is a physical oceanographic term representing the mean wave height of the highest third of the waves. Based on the wave profile data, the dominant wave period is obtained from the frequency domain analysis, and the power generation over 365 days is then estimated, as shown in Fig. 7. The average harvested power is 57.7 W, which is much more than the 12 W peak power consumption of our communication unit, which will be discussed in the next section.

IV. White Space Router Implementation

Our communication units on all the buoys essentially act as wireless routers in a mesh network. Ideally, such a router on the ocean should support high-speed links, have large coverage distance, and be low-cost and low-power. In our work, we built wireless mesh routers that operate on the TV white space band for two reasons.

1) Large Communication Capacity: Although the center frequency of the TV white space is one-fifths of the Wi-Fi band, the available bandwidth in the TV white space is wider than Wi-Fi in the offshore area. For example, the query result from Google's TV white space database [12] for an offshore location 8.4 km away from the shore near Philadelphia (offshore point (39.689934, -74.016235)) shows that 132 MHz bandwidth is available on the TV white space band, while in Philadelphia, the terrestrially available TV white space is only 42 MHz. The amount of TV white space in the offshore area is significant regarding communication capacity since the entire 2.4 GHz Wi-Fi band has only 100 MHz spectrum, and cell phone providers such as Verizon Wireless rely on a mere 114 MHz spectrum to provide broadband wireless service [13].

2) Greater Coverage Distance: Compared to other broadband communication frequencies, TV white space signals can transmit over longer distances because they operate at lower frequencies (*typically*, 470–698 MHz). Specifically, for the same transmit power and antenna gain, the white space band coverage distance is four or five times further than 2.4 GHz Wi-Fi signal. For example, the tens-of-kilometer transmitted range is achieved in practical white space network deployment on the land [14]–[16]. With greater coverage distance, the number of nodes in the mesh network can be reduced. Therefore, a target area can be covered by less energy harvesting buoys and mesh routers, so that the manufacturing and deployment cost is reduced significantly.

However, commercial off-the-shelf white space radios are expensive ($4000–$5000 for a base-station and $1000–$2000 for a client [17]) and also not power-efficient (e.g., for 0.2 W transmit power consumes 25 W of power [18]). The high cost and power significantly limit the scalability of the network and make the practical deployment unlikely. Moreover, since commercial white space radio hardware and software are proprietary, customizing them to the proposed Marinet application is tedious. Therefore, we have designed and implemented a low-cost, low-power white space router prototype, which is customized for use on the ocean. Specifically, we integrated a compact 2.4 GHz low-power Wi-Fi router with an RF front-end to convert the 2.4 GHz frequency signal of the Wi-Fi output to a TV white space band. A light-weight omnidirectional antenna has been designed to transmit/receive signals at the TV white space band. The peak power consumption of the prototyped system is only 12 W for 0.32 W transmit power and 15 W for 0.5 W transmit power.

A. RF Front-End

The main function of the RF front-end is down-conversion and up-conversion between Wi-Fi and white space bands.

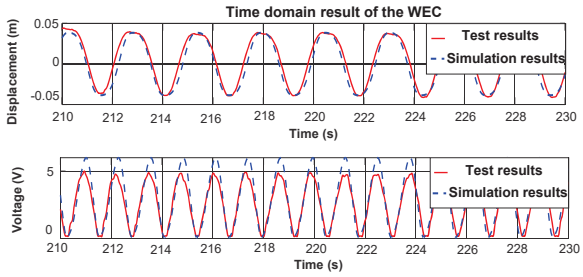

Fig. 5. Test results vs. simulation results of the water tank test.

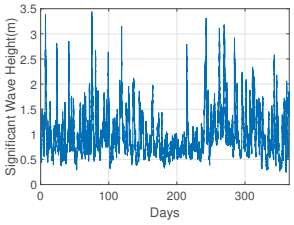

Fig. 6. The wave profile of site 44099 which is about 20 Km away from the coast of Virginia Beach in 2017.

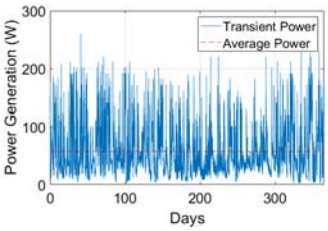

Fig. 7. The Simulated transient power and average power of the WEC during a year.

The simplest form of up/down-conversion is implemented to reduce the overall size and cost. In addition, to increase the communication range, a power amplifier and a low noise amplifier (LNA) are incorporated in the transmit and receive sides, respectively. Fig. 8 shows the detailed block diagram of the RF front-end. As depicted, two mixers are used in the transmitter (top path) and receiver (bottom path) for down-conversion and up-conversion, respectively. The router board used in this project has two pins: the first one is an input/output for 2.4 GHz RX/TX-RF signal, and the second one is a digital pin specifying the status of the board (low for transmit mode and high for receive mode). To use a single antenna in both transmit and receive modes, an RF switch is utilized to separate the transmit and receive paths. The switch is controlled by the digital pin of the router board. In the transmit side, the router RF pin is connected to a variable attenuator to adjust the signal level before feeding it to the mixer. After mixing the signal with a local oscillator (PLL board locked at 1.959 GHz), it is amplified using a driver amplifier followed by a power amplifier. The maximum power delivered to the antenna port is 0.5 W. Low-pass, and band-pass filters are implemented to suppress unwanted harmonics. On the other hand, on the receive side, before up-converting the signal, the LNA is used to increase the received signal level. Then, the up-converted signal is connected directly to the router board. To make the overall structure small, multilayer PCB technology is used in the design of the RF front-end. The overall size of the board is 6.1 cm $\times$ 4.75 cm, and its input voltage is 7 V.

B. White Space Router

As shown in Fig. 10, our low-cost and low-power TV white space router prototype includes seven sub-circuits: the RF front-end, a 2.4-GHz Wi-Fi router, a PLL, a microcontroller, a sensor kit, a microcomputer connected to a camera, and an antenna. In the transmitter side, the output signal of the Wi-Fi router at 2.4 GHz is fed into the RF front-end. The signal is down-converted into a specific available white space band and then transmitted. On the receiver side, the RF front-end up-converts the received signal at the white space band to the 2.4 GHz frequency band, and after filtering, delivers the signal to the Wi-Fi router. The microcontroller receives commands from the router to control the PLL for dynamic channel selection in the TV white space band. It also controls the sensors to send real-time streaming data back to the router for processing. The sensor kit includes a GPS receiver, an inertial measurement unit (accelerometer, gyroscope, and magnetometer), and barometric pressure sensors. This kit monitors the ocean environment by providing information such as real-time motion, temperature, humidity, and pressure. A Raspberry Pi as a microcomputer connected to a camera streams surveillance video to the router via Ethernet cable. The total cost for the prototype is around $523, which is ten times cheaper than the commercial off-the-shelf white space routers. This low-cost white space router significantly reduces the deployment cost of the proposed maritime mesh network. Moreover, the prototyped router supports high transmission power (currently set at 25 dBm) for long-distance communication. Measurement results show the maximum power consumption of the entire router is only 12 W when the RF transmit power is set to 25 dBm, which is less than half the power consumed by commercial off-the-shelf white space routers. It provides a large margin of power budget, given the power harvested by the energy harvesting unit. These results confirm the feasibility of our white space router for the energy harvesting mesh network application. It worth mentioning that the Sleeve Dipole antenna as a simple, low-cost, and low-weight structure is used for link communication. This antenna has an omnidirectional pattern with 2 dBi gain, and it can be replaced by a higher gain antenna [19] to improve the performance of the link.

The router runs a customized version of OpenWrt [20], which is an open-source Linux distribution for embedded devices. OpenWrt provides an interface for flexible channel bandwidth configurations of 5, 10, and 20 MHz, which can appropriately fit into TV channels with 6 MHz bandwidth/channel.

V. Maritime Mesh Networking

As mentioned in Section III and Section IV, the prototypes of the energy harvesting unit and the wireless router unit maintain the feasibility for broadband connection between two remote buoys. Nevertheless, in order to guarantee the stable operation of a large mesh network, the way of handling the link stability issue under rough sea states is a critical challenge for Marinet.

A. Stability Challenges for Marinet

Compared with traditional terrestrial mesh networks, one unique challenge for Marinet is the intrinsic link dynamics under rough weather situations. On land, the mesh nodes are usually mounted on the roof of tall buildings. Hence, they

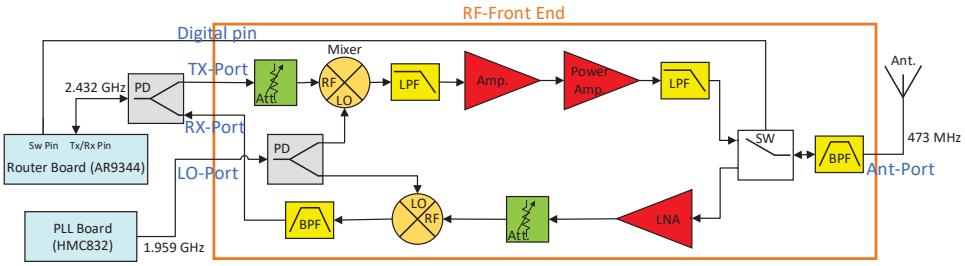

Fig. 8. RF front-end block diagram.

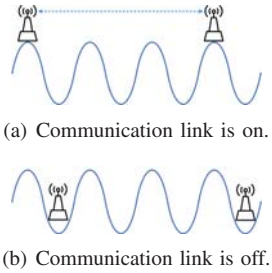

(a) Communication link is on.

(b) Communication link is off.

Fig. 9. Unstable communication link caused by a dynamic ocean wave.

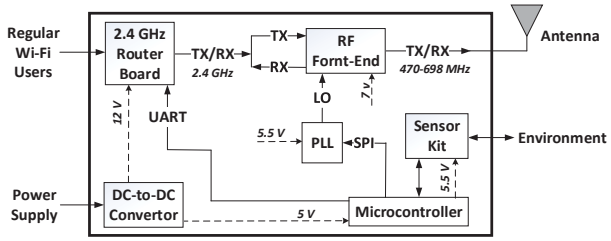

(a) White space router schematic.

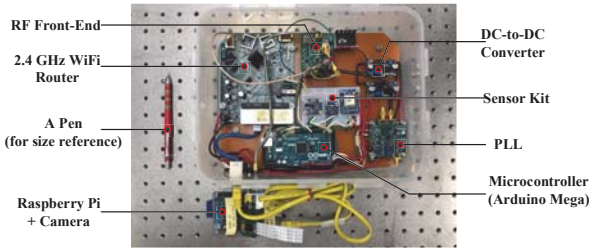

(b) Prototyped white space router.

Fig. 10. White space router.

can maintain stable line-of-sight communication links between each other. However, small-sized floating buoys cannot support such high antennas due to physical stability requirements. Therefore, as the ocean becomes rough, the communication links are affected by the instant heights of both the transmitting/receiving antennas and the waves between them, as shown in Fig. 9. This situation might cause quality degradation or even temporary blockage for the communication links. In a mesh network, such unstable links can cause long packet delays and also affect the convergence of routing algorithms. Without carefully designed solutions, the entire mesh network might not work under rough sea states.

In order to handle this challenge, we developed a link-state prediction algorithm for Marinet. Briefly speaking, the algorithm derives the buoy heights based on the sensor readings. Using the historical and current buoy height measurements, machine learning techniques are applied to predict antenna height in the next few seconds, which are then converted to link-state prediction. In this section, we describe the details of the link-state prediction algorithm.

It is important to note that our contribution focuses on the marine link-state prediction algorithm. We argue that there are already numerous existing adaptive routing and scheduling algorithms that make their routing/scheduling decisions based on link-state prediction [21]. These existing prediction-based routing/scheduling schemes are often found in the fields of mobile ad hoc networks and vehicular ad hoc networks, although their link-state prediction part is not applicable in marine networks. Thus, by integrating our marine link-state prediction algorithm with these existing adaptive routing/scheduling schemes, we can make them applicable to Marinet.

B. Measurement of Buoy Height

A low-cost accelerometer is integrated into every buoy to measure buoy displacement. Since accelerometer can only measure acceleration instead of displacement, we compute the integral of acceleration to obtain speed and then calculate the integral of speed to obtain displacement.

Due to inaccuracies in accelerometer measurement, during these two integrations, errors will be accumulated and amplified, resulting in the drift of final buoy displacement result that completely overshadows the real movement of buoys, as shown by the "displacement before filtering" subfigure in Fig. 11. To address this problem, through spectrum analysis, we discovered that the drift in displacement is dominated by low frequencies. Thus, we applied a high pass digital filter to filter out the low-frequency signals in 0-0.1 Hz. We tested the results of the filtering using an oscillation generator so that we could compare the filtered results with the ground truth provided by the oscillation generator. The filtering algorithm works very well, as shown in Fig. 11, where the ground truth of oscillation matches perfectly with the displacement sensing data after the filtering.

C. Prediction of Buoy Heights

According to the history of buoy displacement measurements, our algorithm then predicts the future of buoy displacement using an appropriate machine learning algorithm. Our selection of the best learning algorithm is not blind. Instead, assuming that the buoy movement is the same as the movement of ocean surface displacement, we conduct a formal analysis of ocean waves to identify the proper learning algorithm.

First, we observe that oceanography studies have already revealed that ocean waves can be described by the linear wave theory, which is widely accepted as an accurate model of ocean waves in deep water based on extensive real-world wave measurement data [22]–[25]. It states that the stochastic process of ocean surface displacement at a given location can

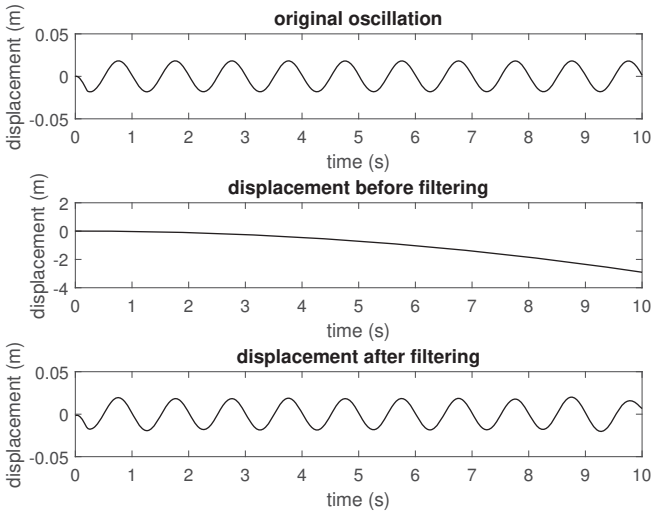

Fig. 11. Filtered sensing results vs. ground truth of displacement (labeled as original oscillation)

be modeled as a linear combination of independent sinusoid waves as follows:

$$F(t) = \sum_{i=1}^{n} A_i \sin(\omega_i t + \theta_i), \tag{1}$$

where t is time. Random variables θ_i, w_i, and A_i represent different phases, frequencies, and amplitudes of the sinusoid waves, respectively. We can simplify the above expression as

$$F(t) = \sum_{i=1}^{n} A_i f_i(t), \text{ where} f_i(t) = \sin(\omega_i t + \theta_i). \tag{2}$$

Assuming the current time is t, samples of the past history of $F(t)$ can be expressed as:

$$F(t - k\epsilon) = \sum_{i=1}^{n} A_i f_i(t - k\epsilon) \text{ for } k \in \{0, 1, ..., M\} \tag{3}$$

where ϵ is the sampling interval of the history, and M is the total number of samples. In addition, note that a single sinusoid has the following property:

$$\begin{aligned} \sin(w_i(t+\delta) + k_i x + \theta_i) &= \cos(\omega_i \delta)\sin(\omega_i t + k_i x + \theta_i) \\ &+ \sin(\omega_i \delta)\sin(\omega_i(t - \frac{\pi}{2\omega_i}) + k_i x + \theta_i). \end{aligned} \tag{4}$$

$$\iff f_i(t+\delta) = \alpha_i(\delta) f_i(t) + \beta_i(\delta) f_i(t - \gamma_i) \tag{5}$$

where $\alpha_i(\delta) = \cos(w_i\delta), \beta_i(\delta) = \sin(w_i\delta)$, and $\gamma_i = \frac{\pi}{2w_i}$. Combining (5) with (2), the future of ocean surface displacement at a fixed point can be expressed as:

$$\begin{aligned} &F(t+\delta) = \sum_{i=1}^{n} A_i f_i(t+\delta) \\ &= \sum_{i=1}^{n} A_i \alpha_i(\delta) f_i(t) + \sum_{i=1}^{n} A_i \beta_i(\delta) f_i(t - \gamma_i) \\ &\approx \sum_{i=1}^{n} A_i \alpha_i(\delta) f_i(t) + \sum_{i=1}^{n} A_i \beta_i(\delta) f_i(t - k_i\epsilon), \end{aligned} \tag{6}$$

where we assume M is large enough and ϵ is fine enough such that every γ_i in (6) can find a corresponding integer k_i such that $k_i\epsilon \approx \gamma_i$. We can treat the set of all $f_i(t - k_i\epsilon)$ and $f_i(t)$ in (6) as a basis of a $2n$ dimensional vector space, a.k.a. $B = \{f_i(t - k_i\epsilon), f_i(t) | i \in \{0, 1, ..., n\}\}$. With such an interpretation, (6) shows that the future of ocean surface displacement is a linear combination of the basis B. Equation (3) shows the relationship between B and another

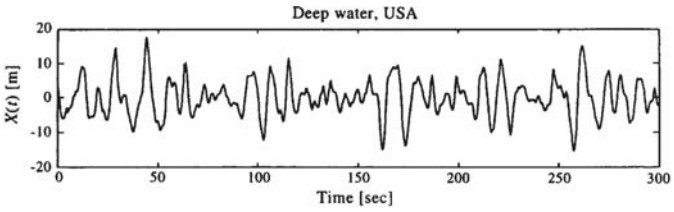

Fig. 12. Real ocean surface movement measurement from [26], which was originally supplied by M. Olagnon, IFREMER, France, and P. Palo, US Naval Facilities Engineering Service Center.

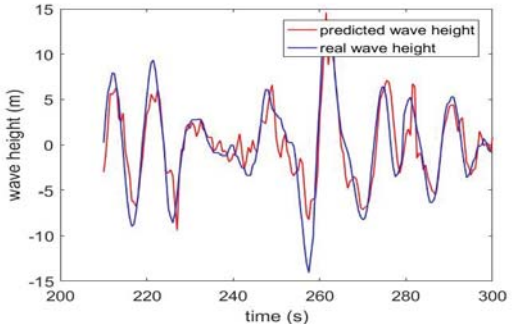

Fig. 13. Prediction accuracy of the multiple linear regression model.

M dimensional basis $C = \{F(t - k\epsilon) | k \in \{0, 1, ..., M\}\}$. Since $M >> n$, basis B is a subset of basis C. According to linear algebra's change of basis computation, the future ocean surface displacement, hence, can be expressed by basis C as:

$$F(t+\delta) = \sum_{k=0}^{M} w_k(\delta) F(t - k\epsilon), \tag{7}$$

where $w_k(\delta)$ are some unknown coefficients. Equation (7) is the standard relationship where the fast and simple multiple linear regression method can be applied so that historical data of $F(t)$ is used to learn w_k. We also vary different values of ϵ and M during the training process to find the optimal sample interval (ϵ) and sampling number (M) based on the past history of $F(t)$.

Using the above multiple linear regression method, we are able to build a very simple and accurate prediction model for displacement. Fig. 12 shows the 300 seconds of real ocean wave movement data. We divide the data into two parts. The first 200 s of data is used to train the multiple linear regression model to obtain w_k, ϵ, and M and the last 100 s data is used to test the model's performance. The prediction lead time δ is set to 5 s. Fig. 13 shows the prediction results. Table I further compares the prediction accuracy of our algorithm, marked as mlr (multiple linear regression), with a few neural network algorithms and a harmonic regression algorithm under different prediction lead time (δ) setting. The prediction accuracy is measured by the Pearson correlation coefficient, where a value of 1 means a perfect match between predictions and actual values. As can be seen, since our mlr-based prediction algorithm is selected based on a proven model of ocean wave movements, its performance is persistently much better than the other machine learning options.

TABLE I
PREDICTION ACCURACY (THE CORRELATION COEFFICIENT BETWEEN PREDICTION AND REAL VALUE*100%) OF OCEAN SURFACE DISPLACEMENT [27]

Method	δ				
	5s	8s	10s	13s	15s
mlr	90.95	87.59	83.25	76.15	72.41
elman	87.31	82.26	75.28	68.59	61.47
newff	81.05	77.82	73.59	66.77	61.06
cascadeforwardnet	84.91	80.73	74.64	66.94	61.16
newfftd	73.79	66.15	62.17	52.33	46.83
newgrnn	70.89	63.47	57.36	46.27	38.62
newrb	54.45	49.61	46.51	37.82	32.63
newrbe	40.81	34.18	31.83	22.7	15.8
harmonic regression	24.06	21.38	19.24	15.88	12.05

D. Link-State Prediction Based on Buoy Heights

With the predicted buoy displacement information, the next step is to map this information to link-state prediction. In this work, we use ocean wave simulation to find out the relationship between buoy displacement and link status. Specifically, we assume that the communication link between two buoys is broken if the sea surface between them blocks the line-of-sight link between them. Then, a realistic simulator of ocean waves in both the time and space domain can provide statistics of such link break probability corresponding to different buoy distance, buoy heights, and the long-term wind speed.

In our study, we use the semi-empirical method outlined in [28] to create realistically simulated ocean waves between a pair of buoys. The first step is to build an ocean wave model for a $L_x \times L_y$ rectangular ocean area. Note that according to linear wave theory, for a location $\mathbf{x} = (x, y)$ in this area, its ocean surface displacement at time t, denoted as $F(\mathbf{x}, \mathbf{t})$, can be represented as the sum of sinusoids with complex and time-independent amplitudes:

$$F(\mathbf{x}, t) = \mathrm{Re}\{\textstyle\sum_{\mathbf{k}} \widetilde{F}(\mathbf{k}, t) \exp(i\mathbf{kx})\}, \tag{8}$$

where $\mathbf{k}$ is a two-dimensional vector $\mathbf{k} = (\mathbf{k_x}, \mathbf{k_y})$, $k_x = 2\pi n/L_x$, $k_y = 2\pi m/L_y$, $-N/2 \leq n \leq N/2$, and $-M/2 \leq m \leq M/2$. Given the spectrum expression of ocean wave $\widetilde{F}(\mathbf{k}, t)$, the temporal ocean surface displacement $F(\mathbf{x}, t)$ can be computed by IFFT (inverse fast Fourier transform) algorithm. Demonstrated by statistical analysis of real ocean monitoring data, $\widetilde{F}(\mathbf{k}, t)$ are nearly statistically stationary, independent, Gaussian fluctuations. Mathematically,

$$\widetilde{F}(\mathbf{k}, t) = \widetilde{A}(\mathbf{k}) \exp(i\omega t) + \widetilde{A}^*(-\mathbf{k}) \exp(-i\omega t), \tag{9}$$

where $\omega = \sqrt{g|\mathbf{k}|}$ in deep water and $*$ is the conjugate operation. $\widetilde{A}(\mathbf{k})$, which are the Fourier amplitudes of a wave height field, are expressed by:

$$\widetilde{A}(\mathbf{k}) = 1/\sqrt{2}(\xi_r + i\xi_i)\sqrt{P(\mathbf{k})}, \tag{10}$$

where ξ_r and ξ_i are independent random numbers with a Gaussian distribution $N(0, 1)$. Empirical analysis of real ocean data has shown that:

$$P(\mathbf{k}) = \frac{C}{|\mathbf{k}|^4} \exp(\frac{-g^2}{|\mathbf{k}|^2 V^4})(\frac{\mathbf{k}}{|\mathbf{k}|}\mathbf{d}), \tag{11}$$

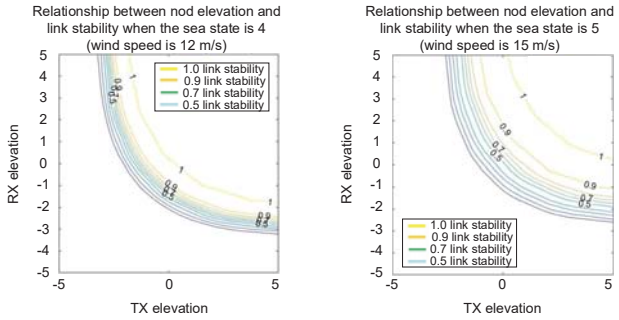

(a) wind speed = 12 m/s (b) wind speed = 15 m/s

Fig. 14. Relationship between transmitter/receiver heights and link stability in different sea states. *Link stability* $= 1 -$ *link blocking probability* and link distance=5km.

where C is a scaling constant, g is the gravitational constant, V is the wind speed, and $\mathbf{d}$ is the wind direction.

Through the above semi-empirical ocean surface simulation, we are able to create dynamic and realistic ocean surface movements between a pair of buoys. We then use the ocean surface simulations to estimate the relationship between buoy heights and link stability. Fig. 14 shows the simulation results for 12 m/s and 15m/s wind speeds, where the probability that the link is alive with respect to different transmitter and receiver heights are shown. It can be seen that the link stability, as shown in Fig. 14, is a function of the elevation of the transmitter and receiver as well as the wind speed. When two communicating buoys' heights are in the upper right corner area enclosed by the 1.0 link stability line, the communication link is fairly stable and has no risk of link breaks.

The simulation-derived function that maps transmitter/receiver heights to link stability can be computed offline and stored at each buoy as a look-up table. Then, a buoy can predict its future link-state by searching the link stability value corresponding to the predicted future heights of itself and its communication peer.

VI. EVALUATION

We used both field experiments and simulations to evaluate various units of the Marinet. The field experiment focused on a single link performance in a small-scale two-buoy scenario. The simulation was used to examine the performance of a large-scale ocean mesh network.

A. Link Measurement

In this section, the measurement results for single-link performance on the water are described. The measurements represent the performance of access links, including received signal strength and throughput over a range of distance. By comparing the measured data with theoretical models, we find a path loss exponent, which can cursorily determine the range and reliability of the mesh links. Furthermore, we introduce an empirical mapping between signal power and achievable throughput to evaluate the throughput of the single-link.

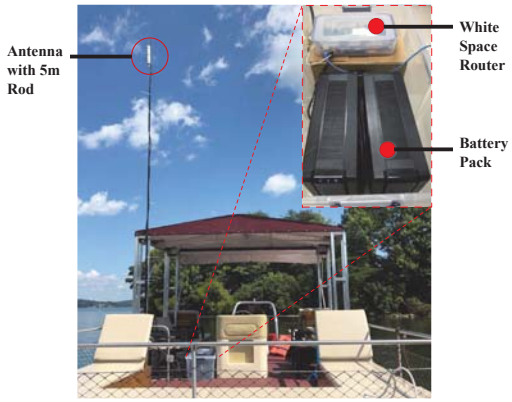

Fig. 15. Experiment setup for field measurements.

1) Experiment Setups: Fig. 15 shows the system setup. Two routers are placed on two sides of a lake with 500 m line-of-sight as the initial separation distance, which then gradually increased to 1500 m during the measurement process. Two routers are configured to establish an 802.11g mesh backhaul link between each other as well as stream sensor data and surveillance video. According to the available white space spectrum database, TV channel 14 with a center frequency of 473 MHz and a bandwidth of 5 MHz is used for link measurement. The transmit power of each router is set to 25 dBm, and the Sleeve dipole antennas are mounted on the top of the 5-meter rods.

2) Data Collection Process: We have configured a real-time monitoring system to display and log the required data from driver and sensors, including the received signal strength indicator (RSSI), modulation coding scheme (MCS), round-trip (RTT) delay, UDP throughput, and packet error rate (PER). A fusion of these data enables the router to monitor link quality and ocean environment in real-time, which are very useful for adaptive network control.

3) Use of the Data: The wireless channel propagation model usually considers three factors: path loss, shadowing, and multipath fading. In our measurement, we focus on deriving the path loss exponent using the measured data, which reflects the impact of distance on signal attenuation over open waters. We have neglected the effect of shadowing because there is almost no obstruction in the experiment field. Multipath fading is not measured in this experiment since it creates rapid signal strength fluctuations that cannot be recorded by our receiving device. Essentially, we assume the received signal strength P_{dBm} fits the following equation:

$$P_{dBm}(d) = P_{dBm}(d_0) - 10\alpha \log_{10}(d/d_0), \qquad (12)$$

where α is the path loss exponent, d is the distance between the transmitter and receiver, and d_0 is a reference distance where we have a measured power level. We use the measurement data to derive α.

4) Measurement Results: Fig. 16 depicts 567 signal strength measurements with respect to various link distance. Using this set of measurements, the empirical path loss exponent in (12) is estimated to be α= 2.8329, and the theoretical curve of (12) matches very well with the measurement.

TABLE II
NS3 SIMULATION PARAMETERS.

Transmission power	25 dBm
Transmitter/receiver gain	10 dBi
Height of antenna	5 m
Packet configuration	100 pkt/s, 1200Bytes/pkt
Node distance	5000 m
Total simulation time	45 s
Transport Layer	UDP
Network Layer	IP & OLSR or our routing protocol
Data-link Layer	Spatial TDMA, 802.11g
Physical Layer	20MHz Bandwidth OFDM
	Center Frequency: 600 MHz

Fig. 17 shows the distribution of field measurements around the theoretical path loss model, which roughly matches a normal distribution with 1.99 dBm standard deviation. With this model, it can be seen that for every 8.5 dB increase in the transmit power or antenna gain, we can double the communication distance between two buoys. We also measure the UDP throughput as a function of signal strength, as shown in Fig. 18. It can be observed that the throughput can be approximated as a piece-wise linear function that is zero at all signal powers below -87 dBm and reaches a ceiling of approximately 6 Mb/s at -62 dBm. The minimum signal power at which we attain a mean throughput of 1 Mb/s is approximately -83 dBm.

B. Sea States and Link Stability Relationship

To analyze the relationship between sea states and wireless link stability, we use NS3 simulation and the ocean surface simulation described in Subsection V-D. In the simulations, we assume that each buoy will be floating on the ocean with its anchor, and hence the x and y coordinates of each buoy are approximately modeled as constants. The z coordinate, which is the elevation of each buoy, is determined by ocean wave motion. Table II shows the parameter settings in the simulation. We implemented spatial TDMA [29] in the MAC layer, which provides collision-free assignments of transmission slots to nodes in a mesh network.

Sea state is a scale used to measure wave height, and each state has an expected wind speed range. With 5 km node distance and 5 m antenna height setting, we simulated 1024 communication links and calculated the link stability averaged over 100 s under 6 sea states. The result is shown in Table III. If the wind speed is less than or equal to 10m/s, the ocean wave will not block any communication links. However, if the wind speed is greater or equal to 15 m/s, the link is likely not working most of the time due to the high blockage rate. This experiment indicates that when wind speed is larger than 10 m/s, marine wireless link faces frequent breakage problems, and adaptive routing/scheduling algorithms based on link-state prediction are necessary to ensure the stable operation of the network.

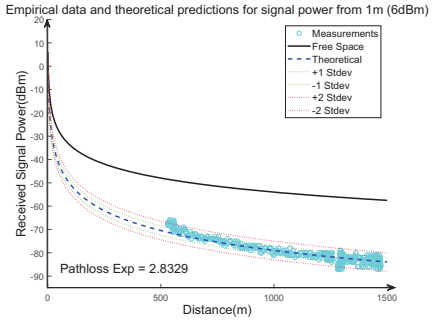

Fig. 16. Empirical data and theoretical predictions for signal power received from 1 meter.

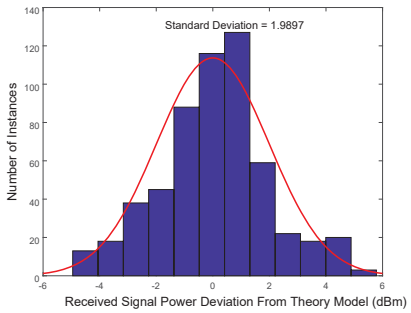

Fig. 17. Empirical distribution of received power around the theoretical path loss

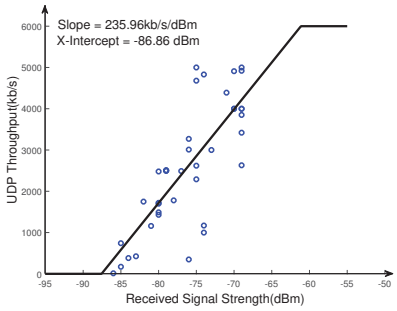

Fig. 18. Measured UDP throughput received by a router as a function of signal strength with a piecewise linear approximation.

C. Flow Throughput Under Link-State-Aware Routing

In this experiment, we demonstrate how our marine link-state prediction can help routing protocol to improve its performance over the marine network. We take the Optimized Link State Routing (OLSR) Protocol [30] as the example routing protocol, where each node will broadcast its link information, and each node will calculate the routing path independently. To combine OLSR with our marine link-state prediction algorithm, we assume embedded sensors on each buoy will measure the wind speed and record the node displacement data (see Subsection V-B). Then, based on the historical elevation information, each node will predict its displacement in the next 5 s time, which is called predicted node elevation information (PNEI). Then, PNEI is added to the Hello message to transmit to neighboring nodes. After receiving Hello messages from its neighbors, the receiver node will calculate the future link stability according to the sea states and the PNEI of itself and its neighbors following the table lookup procedure described in Subsection V-D. When the predicated link stability is lower than a certain threshold, the link is marked as unavailable in OLSR. Otherwise, the link is marked to be available.

We use a simulation of the maritime mesh network in NS3 to evaluate how our link-state prediction algorithm helps OLSR routing system performance. Fig. 19 shows the sample network topology in the simulation. Node 0 is the source node, and node 15 is the destination node for all the traffic. The wind speed is set to 12 m/s. The rest of the settings are the same as in Table II. Table IV compares the throughput under original OLSR and OLSR with our link-state prediction algorithm, respectively, where we vary the link stability threshold values. Under the original OLSR, the throughput is much lower due to frequent link breaks caused by wave movements. Using our link-state prediction algorithm, the number of such link breaks are greatly reduced, and the throughput is improved. In addition, the best link stability threshold turns out to be 1.0, which is reasonable considering that any link break on an active path can create long interruptions for a flow.

VII. Conclusion

In this paper, we explored the feasibility of building a marine wireless mesh network as a means of addressing the network access issues in the offshore area. Through prototype building, field experiments, and simulation, we have demonstrated that such a system is highly feasible. The prototyped ocean-wave energy harvesting buoy can produce an average power of 57.7 W, which is significantly higher than 12 W peak power consumption of the prototyped white space wireless unit and hence guarantees the adequacy of power supply for the router prototype. The network and ocean surface simulation also showed that we could even improve the stability of wireless communications in the rough and dynamic sea states through the use of link-state prediction based on modeling of ocean surface movements. We believe that the marine wireless mesh network is a promising new wireless system design direction that can bring drastic changes to the ocean communication paradigms.

TABLE III
Sea State and Link Stability Relationship.

Wind Speed(m/s)	Significant Wave Height(m)	Sea State	Link Stability
<= 10	<=2.13	Fresh breeze	100.00%
11	2.58	Strong breeze	97.93%
12	3.07	Strong breeze	87.38%
13	3.60	Strong breeze	69.54%
14	4.18	Moderate gale	51.31%
15	4.80	Moderate gale	36.07%

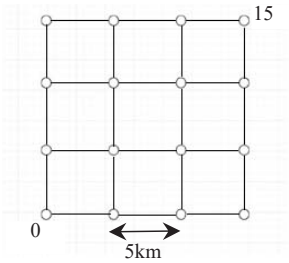

Fig. 19. Network topology.

TABLE IV
Throughput Comparison

Protocol	Threshold	# of received pkts
OLSR with link-state prediction	1.0	4013
	0.9	3907
	0.7	3405
	0.5	3282
original OLSR		3180

Acknowledgment

This material is based upon work supported by the National Science Foundation under Grant No. 1527239 and 1547366.

REFERENCES

[1] K. A. Yau, A. R. Syed *et al.*, "Maritime networking: Bringing internet to the sea," *IEEE Access*, vol. 7, pp. 48 236–48 255, 2019.

[2] S.-W. Jo and W.-S. Shim, "Lte-maritime: High-speed maritime wireless communication based on lte technology," *IEEE Access*, vol. 7, pp. 53 172–53 181, 2019.

[3] G. M. Networks, "Satellite Internet at sea: Hardware, airtime, and pricing," http://www.globalmarinenet.com.

[4] KEYCDN, "The growth of web page size," https://www.keycdn.com.

[5] J. V. Radio, https://www.javad.com/jgnss/products/radios/vhf.html.

[6] T. Hornyak, "Google's 60tbps Pacific cable welcomed in Japan," https://www.computerworld.com/article/2939316, June 2015.

[7] J. Falnes, "Wave-energy conversion through relative motion between two single-mode oscillating bodies," *J. Offshore Mech. and Arctic Engr.*, vol. 121, no. 1, pp. 32–38, 1999.

[8] A. Falcao, "Wave energy utilization: A review of the technologies," *Renew. Sust. Energ. Rev.*, vol. 14, no. 3, pp. 899–918, Apr. 2010.

[9] X. Li, C. Liang, and L. Zuo, "Design and analysis of a two-body wave energy converter with mechanical motion rectifier," *ASME Int. Design Engr. Tech. Conf.*, 2016.

[10] D. Martin, X. Li *et al.*, "Numerical analysis and wave tank validation on the optimal design of a two-body wave energy converter," *Renewable Energy*, vol. 145, pp. 632–641, 2020.

[11] "National Oceanic and Atmospheric Administration's," https://www.ndbc.noaa.gov/.

[12] GOOGLE, "Google spectrum database," https://www.google.com/get/spectrumdatabase/.

[13] M. Dano, "In 2017, how much low-, mid- and high-band spectrum do Verizon, AT&T, T-Mobile, Sprint and Dish own, and where?" https://www.fiercewireless.com, May 2017.

[14] S. Roberts, P. Garnett, and R. Chandra, "Connecting Africa using the TV white spaces: from research to real-world deployments," *The 21st IEEE Int. WKSH. on Local and Metro. Area Networks*, 2015.

[15] A. Hosseini-Fahraji, K. Zeng, Y. Yang, and M. Manteghi, "A self-sustaining maritime mesh network," *USNC-URSI Nat. Radio Science Meeting (NRSM)*, 2019.

[16] R. Campos, T. Oliveira *et al.*, "Bluecom+: Cost-effective broadband communications at remote ocean areas," *OCEANS*, vol. 7, pp. 1–6, 2016.

[17] A. Kumar, A. Karandikar *et al.*, "Towards enabling broadband for a billion plus population with TV white spaces," *IEEE Comm. Mag.*, vol. 54, no. 7, pp. 28–34, 2016.

[18] 6HARMONICS, "GWS 4000 series rural broadband solution."

[19] A. Hosseini-Fahraji and M. Manteghi, "Design of a wideband coaxial collinear antenna," *2019 IEEE Int. Symp. Ant. and Propag. and USNC-URSI Radio Sci. Meeting*, 2019.

[20] OpenWRT, https://openwrt.org/.

[21] I. Akyildiz and X.Wang, *Wireless mesh networks*. Wiley, 2009.

[22] S. R. Massel, *Ocean surface waves: their physics and prediction*. World Scientific, 2013, vol. 36.

[23] L. H. Holthuijsen, *Waves in oceanic and coastal waters*. Cambridge Uni. press, 2010.

[24] M. K. Ochi, *Ocean waves: the stochastic approach*. Cambridge Uni. Press, 2005, vol. 6.

[25] A. Shahanaghi, Y. Yang, and R. M. Buehrer, "On the stochastic link modeling of static wireless sensor networks in ocean environments," *IEEE Conference on Computer Communications (INFOCOM)*, 2019.

[26] I. Rychlik, P. Johannesson, and M. Leadbetter, "Modeling and statistical analysis of ocean-wave data using transformed gaussian processes," *Marine Structures*, vol. 10, no. 1, pp. 13–47, 1997.

[27] S. Yu, "Ocean wave simulation and prediction," Master's thesis, Virginia Polytechnic Institute and State University, 2018.

[28] J. Tessendorf, "Simulating ocean water," *Simulating nature: realistic and interactive techniques. SIGGRAPH*, vol. 1, no. 2, p. 5, 2001.

[29] R. Nelson and L. Kleinrock, "Spatial TDMA: A collision-free multihop channel access protocol," *IEEE Tran. on Communications*, vol. 33, no. 9, pp. 934–944, 1985.

[30] T. Clausen and P. Jacquet, "Optimized link state routing protocol (olsr)," https://tools.ietf.org/html/rfc3626, 2003.